Dynamic State Estimation for DFIG with Unknown Inputs Based on Cubature Kalman Filter and Adaptive Interpolation

Maolin Zhu, Hao Liu, *Member*, *IEEE*, Junbo Zhao, *Senior Member*, *IEEE*, Bendong Tan, *Student Member*, *IEEE*, Tianshu Bi, *Fellow*, *IEEE*, and Samson Shenglong Yu, *Member*, *IEEE*

***Abstract*—Dynamic state estimation (DSE) accurately tracks the dynamics of power systems and demonstrates the evolution of the system state in real time. This paper proposes a DSE approach for a doubly-fed induction generator (DFIG) with unknown inputs based on adaptive interpolation and cubature Kalman filter (AICKF-UI). DFIGs adopt different control strategies in normal and fault conditions; thus, the existing DSE approaches based on the conventional control model of DFIG are not applicable in all cases. Consequently, the DSE model of DFIGs is reformulated to consider the converter controller outputs as unknown inputs, which are estimated together with the DFIG dynamic states by an exponential smoothing model and augmented-state cubature Kalman filter. Furthermore, as the reporting rate of existing synchro-phasor data is not sufficiently high to capture the fast dynamics of DFIGs, a large estimation error may occur or the DSE approach may diverge. To this end, in this paper, a local-truncation-error-guided adaptive interpolation approach is developed. Extensive simulations conducted on a wind farm and the modified IEEE 39-bus test system show that the proposed AICKF-UI can ① effectively address the divergence issues of existing cubature Kalman filters while being computationally more efficient; ② accurately track the dynamic states and unknown inputs of the DFIG; and ③ deal with various types of system operating conditions such as time-varying wind and different system faults.**

***Index Terms*—Adaptive interpolation, cubature Kalman filtering, doubly-fed induction generator (DFIG), dynamic state estimation, unknown input.**

I. Introduction

WIND energy has attracted significant attention in recent years owing to its renewability, easy availability, and environmental friendliness. Accordingly, the penetration of wind generation is rapidly increasing in power systems around the world. Consequently, doubly-fed induction generators (DFIGs) have been widely deployed owing to their good controllability and high efficiency [1]. However, their intermittency and dynamic responses during transient events have a substantial impact on secure system operation. This requires the development of innovative dynamic monitoring tools such as the dynamic state estimation (DSE) approaches using fast and synchronized measurements from phasor measurement units (PMUs) [2], [3].

Most existing DSE approaches are developed for traditional synchronous generators [4]-[6]. However, the complexity of wind generators has increased from the modeling perspective, particularly in terms of power electronics and related controllers [7]. An appropriate dynamic model of DFIGs is critical for the DSE. In [8] and [9], the conventional control of DFIGs is modeled using the DSE, but fault control strategies [10], [11] are ignored. However, when a fault occurs, the transient dynamic process of DFIGs under the fault control strategies plays an essential role in affecting the power system dynamics, and thus should be effectively captured by the DSE [12]. In addition, in the event of a serious fault, some protection circuits such as crowbars are used to prevent overcurrent situations [13]. To solve this problem, a general DSE framework for permanent magnet synchronous generator (PMSG) -based wind generation is proposed in [14]. This framework decouples the generator model from the controllers in a PMSG but assumes that the outputs of the converter controller are measured or available in the DSE; however, this may not be practical because the DSE is mainly based on the synchronous measurement of PMUs [6], which does not include the outputs of the converter controllers.

The most widely used DSE approaches for DFIGs include the extended Kalman filter [15], unscented Kalman filter [8], cubature Kalman filter (CKF) [16], and particle filter [9], [17]. However, the mismatch between the fast dynamics of DFIGs and the existing phasor measurement reporting rate is ignored in these studies. Note that DFIGs generally have a small capacity and the dynamic states of their rotor, DC capacitor, AC windings, and filter inductance have relatively low time constants [18]. Consequently, the state prediction

Manuscript received: January 26, 2023; revised: March 10, 2023; accepted: March 23, 2023. Date of CrossCheck: March 23, 2023. Date of online publication: April 19, 2023.

This work was supported by the National Natural Science Foundation of China (No. 51725702).

M. Zhu, H. Liu (corresponding author), and T. Bi are with the State Key Laboratory of Alternate Electrical Power System with Renewable Energy Sources, North China Electric Power University, Beijing, China (e-mail: mlzhu@ncepu.edu.cn; hliu@ncepu.edu.cn; tsbi@ncepu.edu.cn).

J. Zhao and B. Tan are with the Department of Electrical and Computer Engineering, University of Connecticut, Storrs, 06269, USA (e-mail: junbo@uconn.edu; bt1133@msstate.edu).

S. Yu is with the School of Engineering, Deakin University, 75 Pigdons Road, Waurn Ponds, VIC, 3216, Australia (email: s.yu@ieee.org).

DOI: 10.35833/MPCE.2023.000042

for the DSE approaches may be inaccurate, as the DSE time step is large, e.g., consistent with the PMU reporting rate of 50 or 60 samples per second [19]. To this end, an impractical high sampling rate of 4000 samples per second is assumed in [14], while in [16], pseudo measurements are used to increase the sampling rate by performing a simple measurement interpolation without selection basis for the interpolation parameter. The latter is a viable approach, but the computing time increases due to the interpolation. Thus, it is critical to choose an appropriate interpolation parameter to balance the tradeoff between the computing efficiency and estimation accuracy of the DSE approaches. In numerical analysis and time-domain simulation, an adaptive step size [20] based on the integral difference between two numerical approaches with different accuracy orders is widely used, such as the RKF45 [21]. Considering that the discrete prediction step of the DSE approaches also involves numerical integration, the idea of an adaptive step size can be extended to the measurement interpolation of the DSE approaches for DFIGs.

To address these issues, this paper proposes a DSE approach for a DFIG based on adaptive interpolation and CKF (AICKF-UI). The main contributions of this paper are summarized as follows.

1) The DSE model for DFIGs is reformulated to consider the status of the crowbar and the converter controller outputs as the unknown inputs to cope with the diverse control strategies, significantly increasing the generalizability of the proposed AICKF-UI approach and reducing the model complexity.

2) The unknown inputs are accurately estimated together with the DFIG dynamic states by an exponential smoothing model and a CKF with an augmented state vector, which consider the correlations among the unknown inputs $\boldsymbol{d}_k$, dynamic states $\boldsymbol{x}_k$, and measurements $\boldsymbol{z}_k$.

3) The AICKF-UI approach with the adaptive interpolation parameter is proposed to estimate the states of the DFIG. A local truncation error (LTE)-aware estimation approach is developed to mitigate the discretization error of the prediction step. This is critical during large disturbances, where the existing approaches either yield large estimation errors or diverge.

The remainder of this paper is structured as follows. The reformulated DFIG model with unknown inputs is described in Section II. Section III describes the proposed AICKF-UI approach. Section IV presents case studies and evaluates the performance of the proposed approach on a wind farm and the modified IEEE 39-bus test system. Finally, the conclusions are provided in Section V.

II. DFIG Model with Unknown Inputs

Figure 1 shows the basic structure of the DFIG model coupled with a wind turbine and power grid, where RSC and GSC represent the rotor-side and grid-side converters, respectively; $\boldsymbol{I}_s$ and $\boldsymbol{I}_r$ are the stator and rotor currents, respectively; $\boldsymbol{U}_s$ is the stator voltage; ω_r is the speed of the wind turbine; R_c is the resistance of the crowbar; I_t is the output current of DFIG; U_{dc} is the DC capacitor voltage; F_{CB}^c is the crowbar controller output; $\boldsymbol{U}_r^c$ and $\boldsymbol{U}_g^c$ are the outputs of the converter controllers. The actual circuit connections are shown by solid red lines; the controller outputs are shown by solid blue lines; and the measurements are indicated by black dashed lines. The complete dynamic model of a grid-connected DFIG includes a wind turbine, an asynchronous generator, a set of AC-DC and DC-AC converters with controllers, a grid-side filter, and a crowbar circuit. The wind turbine transfers wind energy to the DFIG through the mechanical shaft. The stator of the induction machine is directly connected to the grid while the rotor is fed through a back-to-back converter.

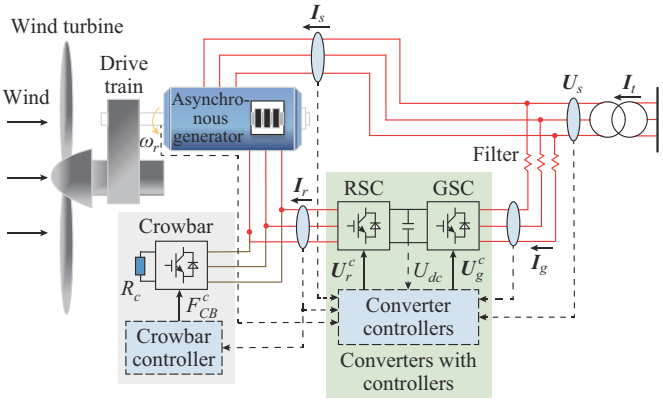

Fig. 1. Structure of DFIG model.

The mathematical model of the DFIG comprising a set of differential and algebraic equations is described below in detail.

A. Wind Turbine

The wind turbine is the primary energy conversion component of the DFIG. It can be described by:

$$\begin{cases} T_m = -P_m/\omega_r \\ P_m = C_p(\lambda,\beta)V_w^3 K_N P_{m,nom}/P_{e,nom} \end{cases} \tag{1}$$

where T_m is the torque of the wind turbine; P_m is the mechanical power; C_p is the mechanical power coefficient, and the detailed mathematical descriptions of C_p are given in [8]; λ is the blade tip ratio; β is the pitch angle of the wind turbine; V_w is the wind speed; K_N is the factor of the output power of the wind turbine; and $P_{m,nom}$ and $P_{e,nom}$ are the nominal mechanical and electric power, respectively.

B. Asynchronous Generator

A single-mass model of the drive train [22] in (2) is adopted to describe the relationships among the rotor speed ω_r, mechanical torque T_m, and electrical torque T_e:

$$\begin{cases} \mathrm{d}\omega_r/\mathrm{d}t = (T_m - T_e - F\omega_r)/2H_g \\ T_e = \psi_{ds} i_{qs} - \psi_{qs} i_{ds} \end{cases} \tag{2}$$

where H_g is the inertia of the generator; F is the friction factor; and ψ_{ds}, ψ_{qs} and i_{ds}, i_{qs} are the d-q components of the stator flux $\boldsymbol{\psi}_s$ and current $\boldsymbol{I}_s$, respectively.

The voltage equations of the generator winding based on

electromotor conventions are expressed as:

$$\begin{cases} \mathrm{d}\psi_{ds}/\mathrm{d}t=\omega_b(u_{ds}+\omega_s\psi_{qs}-R_s i_{ds}) \\ \mathrm{d}\psi_{qs}/\mathrm{d}t=\omega_b(u_{qs}-\omega_s\psi_{ds}-R_s i_{qs}) \\ \mathrm{d}\psi_{dr}/\mathrm{d}t=\omega_b(u_{dr}+(\omega_s-\omega_r)\psi_{qr}-R_r i_{dr}) \\ \mathrm{d}\psi_{qr}/\mathrm{d}t=\omega_b(u_{qr}-(\omega_s-\omega_r)\psi_{dr}-R_r i_{qr}) \end{cases} \tag{3}$$

where the subscripts d and q represent the d-q components of the rotor current $\boldsymbol{I}_r$, rotor voltage $\boldsymbol{U}_r$, stator voltage $\boldsymbol{U}_s$, and rotor flux $\boldsymbol{\psi}_r$, respectively; ω_b is the base angular speed; ω_s is the synchronous angular speed; and R_s and R_r are the stator and rotor resistances, respectively.

The stator currents (i_{ds} and i_{qs}) and the rotor currents (i_{dr} and i_{qr}) can be expressed as:

$$\begin{cases} i_{ds}=(\psi_{ds}-\psi_{dm})/L_{ls} \\ i_{qs}=(\psi_{qs}-\psi_{qm})/L_{ls} \\ i_{dr}=(\psi_{dr}-\psi_{dm})/L_{lr} \\ i_{qr}=(\psi_{qr}-\psi_{qm})/L_{lr} \end{cases} \tag{4}$$

where L_{ls} and L_{lr} are the leakage inductances of the stator and rotor windings, respectively; and ψ_{dm} and ψ_{qm} are the stator-rotor mutual fluxes given by:

$$\begin{cases} \psi_{dm}=\psi_{dr}/(\sigma L_{lr})+\psi_{ds}/(\sigma L_{ls}) \\ \psi_{qm}=\psi_{qr}/(\sigma L_{lr})+\psi_{qs}/(\sigma L_{ls}) \\ \sigma=1/L_{ls}+1/L_{lr}+1/L_m \end{cases} \tag{5}$$

where L_m is the mutual inductance.

C. Converter with Controller

The converter of the DFIG consists of an RSC, GSC, and DC link. As the time constant of the converter is on the order of microseconds, its modulation process can be ignored. Then, the converter outputs $\boldsymbol{U}_r$ and $\boldsymbol{U}_g$ are considered equal to their corresponding control commands, i. e., $\boldsymbol{U}_r^c$ and $\boldsymbol{U}_g^c$. Therefore, the converter controller considerably affects the dynamics of the DFIG, and proper handling of the converter controllers is important in the DSE.

The detailed controller model is considered in [8], [9] for the DSE of the DFIG, but it only involves the conventional control strategies applied to normal conditions. However, when a voltage drop occurs owing to a fault, a series low-voltage ride-through (LVRT) control strategy [10] will be activated to keep the DFIG connected to the power grid. A crowbar circuit will be switched on when a severe voltage drop occurs. Thus, it is inappropriate to only consider the conventional control strategies in the DSE. In addition, the controllers providing instructions based on proportional-integral (PI) control belong to secondary systems, and the integral dynamic states of PI control are not our focus. Consequently, it is difficult and unnecessary to consider the detailed controller model in the DSE.

The converter outputs $\boldsymbol{U}_r$ and $\boldsymbol{U}_g$ are assumed to be available in [14], and the controller impacts can be simply captured by considering them as time-varying known inputs in the DSE. However, the DSE is usually deployed at the main station of a measurement system and uses the synchronous measurements of PMUs [6], where the DFIG terminal voltage and current phasors are measured, but the outputs of the converter controllers are not included. Moreover, the measurements of the DFIGs are usually asynchronous and only used for local control. In addition, for the equivalent model of the wind farm, the converter outputs do not exist, and thus, cannot be measured.

Considering the aforementioned problems, the converter outputs $\boldsymbol{U}_r$ and $\boldsymbol{U}_g$ are considered as the unknown inputs $\boldsymbol{d}$ of the DSE in this paper to deal with the complex control strategies of the DFIG as follows:

$$\boldsymbol{d}=[\boldsymbol{U}_r,\boldsymbol{U}_g]^{\mathrm{T}}=[u_{dr},u_{qr},u_{dg},u_{qg}]^{\mathrm{T}} \tag{6}$$

where u_{dg} and u_{qg} are the d-q components of the grid-side voltage $\boldsymbol{U}_g$, respectively. $\boldsymbol{d}$ is estimated by the proposed approach in Section III. Note that the converter outputs are regarded as unknown inputs only in the DSE, and the simulations performed in a simulation software still adopt the complete DFIG model.

Moreover, the model of the grid-side filter in the d-q frame is given by:

$$\begin{cases} \mathrm{d}i_{dg}/\mathrm{d}t=\omega_b(u_{ds}-u_{dg}-R_g i_{dg}+L_g i_{qg})/L_g \\ \mathrm{d}i_{qg}/\mathrm{d}t=\omega_b(u_{qs}-u_{qg}-R_g i_{qg}+L_g i_{dg})/L_g \end{cases} \tag{7}$$

where i_{dg} and i_{qg} are the d-q components of the grid-side current $\boldsymbol{I}_g$, respectively; L_g is the filter inductance; and R_g is the resistance of the grid-side filter.

D. Crowbar Model

Under the normal condition, the RSC operates normally to regulate the output power of the turbine, as shown in Fig. 2(a). However, when there is a severe voltage drop at the terminal of the DFIG, the transient control strategies based on converter controllers may not guarantee the LVRT ability of the DFIG. Then, the crowbar must be put into operation, and meanwhile, the RSC is locked to maintain the connection of the DFIG to the power grid, as shown in Fig. 2(b). The rotor windings are short-circuited by the crowbar, and the DFIG becomes an asynchronous generator [23]. Hence, this process needs to be considered in the DSE model. F_{CB}, defined as the status of the crowbar, is considered as an input of the DSE. When $F_{CB}=1$, i. e., the crowbar is switched on, the mathematical model of the induction motor must be modified according to the following equation:

$$\begin{cases} u_{dr}=u_{qr}=0 \\ R_r'=R_r+R_c \end{cases} \tag{8}$$

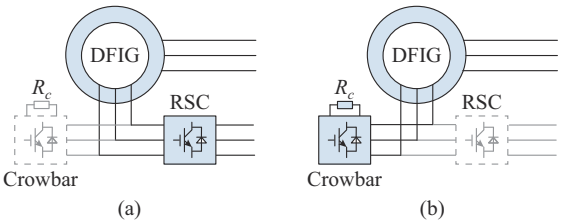

Fig. 2. Cases where crowbar is switched off or on. (a) Crowbar is switched off. (b) Crowbar is switched on.

E. Summary of DSE Model for DFIG

The estimation model of the DFIG can be summarized as

the following general continuous state-space model:

$$\begin{cases} \dot{\boldsymbol{x}} = \boldsymbol{f}_c(\boldsymbol{x}, \boldsymbol{u}) + \boldsymbol{G}_c \boldsymbol{d} + \boldsymbol{w} \\ \boldsymbol{z} = \boldsymbol{h}_c(\boldsymbol{x}, \boldsymbol{u}) + \boldsymbol{v} \end{cases} \tag{9}$$

where $\boldsymbol{f}_c$ is the function that represents the system dynamic equations, including (2), (3), and (7); $\boldsymbol{G}_c$ is the distribution matrix of the unknown input vector; $\boldsymbol{h}_c$ is the function that represents the measurement equations; and $\boldsymbol{w} \in \mathbf{R}^n$ and $\boldsymbol{v} \in \mathbf{R}^m$ are the process and measurement noise, and their corresponding covariance matrices are $\boldsymbol{\Theta}$ and $\boldsymbol{\Lambda}$, respectively, and m and n are the dimensions of $\boldsymbol{z}$ and $\boldsymbol{x}$, respectively. Then, the dynamic state vector $\boldsymbol{x}$, input vector $\boldsymbol{u}$, unknown input vector $\boldsymbol{d}$, and measurement vector $\boldsymbol{z}$ are expressed as:

$$\begin{cases} \boldsymbol{x} = [\omega_r, \psi_{ds}, \psi_{qs}, \psi_{dr}, \psi_{qr}, i_{dg}, i_{qg}]^{\mathrm{T}} = [x_1, x_2, x_3, x_4, x_5, x_6, x_7]^{\mathrm{T}} \\ \boldsymbol{u} = [u_{ds}, u_{qs}, V_w, F_{CB}]^{\mathrm{T}} = [u_1, u_2, u_3, u_4]^{\mathrm{T}} \\ \boldsymbol{d} = [u_{dr}, u_{qr}, u_{dg}, u_{qg}]^{\mathrm{T}} = [d_1, d_2, d_3, d_4]^{\mathrm{T}} \\ \boldsymbol{z} = [P_t, Q_t, i_{ds}, i_{qs}]^{\mathrm{T}} = [z_1, z_2, z_3, z_4]^{\mathrm{T}} \end{cases} \tag{10}$$

where P_t and Q_t are the terminal active power and reactive power measurements, respectively. According to the second-level data record [24], the fluctuation of V_w can be ignored within the DSE execution interval, which is generally the same as the PMU measurement interval, i.e., 0.02 s or shorter. Then, the measurement results of the existing wind speed measurement equipment in the wind farm such as nacelle anemometers and anemometer towers can be used. Thus, it is assumed reasonably that the wind speed V_w can be measured and considered as a known input of the DSE.

Then, the system (9) should be discretized to be suitable for the Kalman filter frame. Considering the balance between the computational efficiency and the accuracy, the second-order Runge-Kutta (2-RK) approach [25] is used in this paper as:

$$\begin{cases} \boldsymbol{x}_k = \boldsymbol{x}_{k-1} + (\Delta \boldsymbol{x}_1 + \Delta \boldsymbol{x}_2)/2 \\ \Delta \boldsymbol{x}_1 = \boldsymbol{f}_c(\boldsymbol{x}_{k-1}) \Delta h \\ \Delta \boldsymbol{x}_2 = \boldsymbol{f}_c(\boldsymbol{x}_{k-1} + \Delta \boldsymbol{x}_1) \Delta h \end{cases} \tag{11}$$

where Δh is the step size. Thus, the discrete model of (9) is expressed as:

$$\begin{cases} \boldsymbol{x}_k = \boldsymbol{f}(\boldsymbol{x}_{k-1}, \boldsymbol{u}_{k-1}) + \boldsymbol{G}\boldsymbol{d}_{k-1} + \boldsymbol{w}_k \\ \boldsymbol{z}_k = \boldsymbol{h}(\boldsymbol{x}_k, \boldsymbol{u}_k) + \boldsymbol{v}_k \end{cases} \tag{12}$$

where $\boldsymbol{f}$ and $\boldsymbol{h}$ are the discrete versions of $\boldsymbol{f}_c$ and $\boldsymbol{h}_c$, respectively. The unknown input distribution matrix $\boldsymbol{G}$ is given in (13), showing the relationship between the dynamic states and the unknown inputs.

$$\boldsymbol{G} = \begin{bmatrix} 0 & 0 & 0 & \omega_b \Delta h & 0 & 0 & 0 \\ 0 & 0 & 0 & 0 & \omega_b \Delta h & 0 & 0 \\ 0 & 0 & 0 & 0 & 0 & -\omega_b \Delta h / L_g & 0 \\ 0 & 0 & 0 & 0 & 0 & 0 & -\omega_b \Delta h / L_g \end{bmatrix}^{\mathrm{T}} \tag{13}$$

As there are unknown inputs in the DFIG state space and they are considered as part of the states in this paper, it is necessary to check whether the selected measurement is reasonable and to analyze the observability of the DFIG system with augmented states. The rank requirement to estimate the unknown inputs is discussed in [26], where the unknown input vector is estimated and then substituted into the dynamic model for a repeated Kalman filter. Specifically, the unknown input vector can be obtained using the following equation:

$$\boldsymbol{d}_k = (\boldsymbol{G}^{\mathrm{T}} \boldsymbol{H}_k^{\mathrm{T}} \tilde{\boldsymbol{R}}^{-1} \boldsymbol{H}_k \boldsymbol{G})^{-1} \boldsymbol{G}^{\mathrm{T}} \boldsymbol{H}_k^{\mathrm{T}} \tilde{\boldsymbol{R}}^{-1} (\boldsymbol{z}_k - \boldsymbol{z}_{k|k-1}) \tag{14}$$

where $\boldsymbol{H}_k$ is the Jacobian matrix of $\boldsymbol{h}_k$; $\tilde{\boldsymbol{R}} = \boldsymbol{H}_k \boldsymbol{\Sigma}_{k|k-1} \boldsymbol{H}_k^{\mathrm{T}} + \boldsymbol{\Theta}$; $\boldsymbol{\Sigma}_{k|k-1}$ is the covariance matrix of the predicted state vector $\boldsymbol{x}_{k|k-1}$; and $\boldsymbol{z}_{k|k-1}$ is the predicted measurement vector. The aforementioned estimation equation for the unknown inputs requires $rank(\boldsymbol{H}_k \boldsymbol{G}) = rank(\boldsymbol{G}) = m$ to make the inversion of the matrix, which is expressed in (14), possible, i. e., the number of measurement outputs m should be at least equal to the number of unknown inputs p. Appendix A provides the expression of $\boldsymbol{H}_k \boldsymbol{G}$ of the DFIG, and the results show that the rank requirement in (14) is satisfied for the DFIG case, and the unknown input vector $\boldsymbol{d}$ can be observed from the selected measurement vector $\boldsymbol{z}$.

System observability is defined as the ability to determine the states of the system uniquely from available measurements [6]. The observability of a dynamical system can be readily determined by whether its observability matrix $\tilde{\boldsymbol{O}}$ in (15) has full rank, i.e., the rank of $\tilde{\boldsymbol{O}}$ is equal to n (the dimension of the state vector).

$$\tilde{\boldsymbol{O}} = [\boldsymbol{H}^{\mathrm{T}}, (\boldsymbol{H}\boldsymbol{F})^{\mathrm{T}}, \ldots, (\boldsymbol{H}\boldsymbol{F}^{n-1})^{\mathrm{T}}]^{\mathrm{T}} \tag{15}$$

where $\boldsymbol{F}$ is the Jacobian matrix of the system dynamic functions. As the unknown inputs are considered as part of the states in this paper, the above approach is considered appropriate for the observability analysis of the augmented states, similar to the approach in [27]. The analysis result in Appendix B shows that the observability matrix $\tilde{\boldsymbol{O}}$ of the DFIG system with augmented states satisfies full-rank requirement, and thus, the augmented states are observable under the selected measurement set.

III. Proposed AICKF-UI Approach

The proposed AICKF-UI approach consists of three key steps: ① an exponential smoothing model for predicting unknown inputs; ② a CKF with an augmented state vector; and ③ adaptive measurement interpolation.

A. Exponential Smoothing Model for Predicting Unknown Inputs

From (3), it can be observed that $\boldsymbol{U}_r$ affects $\boldsymbol{\psi}_r$, which can change $\boldsymbol{\psi}_s$ and $\boldsymbol{I}_s$ through $\boldsymbol{\psi}_m$, and consequently, the stator output power P_s and Q_s relying on $\boldsymbol{I}_s$ can also be affected. $\boldsymbol{I}_g$ is affected by $\boldsymbol{U}_g$ in (7), and thus, the GSC output power P_g and Q_g is also affected. This indicates that $\boldsymbol{d}_k$ has spatial correlations with $\boldsymbol{x}_k$. Moreover, the output power of the stator and GSC affects $\boldsymbol{U}_r$ and $\boldsymbol{U}_g$ in turn through PI feedback control where integral state variables and differential equations exist. Therefore, there are temporal correlations among the time series signals of $\boldsymbol{d}_k$.

For the temporal correlations, the following historical time series $\hat{\boldsymbol{d}}_h$ is used to predict $\boldsymbol{d}_k$ for time step k:

$$\hat{\boldsymbol{d}}_h=\{\hat{\boldsymbol{d}}_{k-T},\hat{\boldsymbol{d}}_{k-T+1},...,\hat{\boldsymbol{d}}_{k-1}\} \tag{16}$$

where $T\geq 2$ is the dimension of the historical time series; and $\hat{\boldsymbol{d}}_{k-i}$ is the estimation of $\boldsymbol{d}_{k-i}$ at time step $k-i$ ($i=1,2,...,T$). In this paper, an exponential smoothing model (ESM) is used to consider the temporal correlations of the time series of unknown inputs [28]. The simplest form of the ESM is given by:

$$\boldsymbol{d}_{k|k-1}=\alpha\hat{\boldsymbol{d}}_{k-1}+(1-\alpha)\boldsymbol{d}_{k-1|k-2}\quad 0<\alpha\leq 1 \tag{17}$$

where α is a smoothing factor. The ESM obtains $\boldsymbol{d}_{k|k-1}$ by assigning different weights to the estimation $\hat{\boldsymbol{d}}_{k-1}$ and forecasts $\boldsymbol{d}_{k-1|k-2}$ at the previous time step $k-1$. Recursively replacing $\boldsymbol{d}_{k-1|k-2}$ with $\boldsymbol{d}_{k-2|k-3}$, $\boldsymbol{d}_{k-3|k-4}$, …, $\boldsymbol{d}_{k-T+1|k-T}$, $\boldsymbol{d}_{k|k-1}$ can be expressed as:

$$\begin{aligned}\boldsymbol{d}_{k|k-1}=&\alpha\hat{\boldsymbol{d}}_{k-1}+(1-\alpha)[\alpha\hat{\boldsymbol{d}}_{k-2}+(1-\alpha)\boldsymbol{d}_{k-2|k-3}]=\\&\alpha\sum_{i=1}^{T-1}(1-\alpha)^{i-1}\hat{\boldsymbol{d}}_{k-i}+(1-\alpha)^{T-1}\boldsymbol{d}_{k-T+1|k-T}\end{aligned} \tag{18}$$

The weight $\alpha(1-\alpha)^i$ of $\hat{\boldsymbol{d}}_{k-i}$ decreases geometrically; hence, the earlier historical data have a smaller contribution to $\boldsymbol{d}_{k|k-1}$, and a greater weight will be given to more recent estimations if α is large (i.e., close to 1). In addition, $\boldsymbol{d}_k$ of the DFIG will inevitably show a trend and periodicity in the dynamic process owing to the PI control of the converter controllers. The single ESM in (17) will exhibit a lag bias and is not suitable for this case. Therefore, multiple smoothing is used to consider the information of lag deviation and enable $\boldsymbol{d}_{k|k-1}$ to follow the trend of the time series. Then, (22) is extended to the following triple ESM:

$$\begin{cases}\boldsymbol{d}^{(1)}_{k|k-1}=\alpha\hat{\boldsymbol{d}}_{k-1}+(1-\alpha)\boldsymbol{d}^{(1)}_{k-1|k-2}\\ \boldsymbol{d}^{(2)}_{k|k-1}=\alpha\boldsymbol{d}^{(1)}_{k|k-1}+(1-\alpha)\boldsymbol{d}^{(2)}_{k-1|k-2}\\ \boldsymbol{d}^{(3)}_{k|k-1}=\alpha\boldsymbol{d}^{(2)}_{k|k-1}+(1-\alpha)\boldsymbol{d}^{(3)}_{k-1|k-2}\end{cases} \tag{19}$$

$$\boldsymbol{d}_{k|k-1}=\boldsymbol{a}_{k|k-1}+\boldsymbol{b}_{k|k-1}+\boldsymbol{c}_{k|k-1} \tag{20}$$

$$\begin{cases}\boldsymbol{a}_{k|k-1}=3\boldsymbol{d}^{(1)}_{k|k-1}-3\boldsymbol{d}^{(2)}_{k|k-1}+\boldsymbol{d}^{(3)}_{k|k-1}\\ \boldsymbol{b}_{k|k-1}=\eta(\kappa_1\boldsymbol{d}^{(1)}_{k|k-1}-\kappa_2\boldsymbol{d}^{(2)}_{k|k-1}+\kappa_3\boldsymbol{d}^{(3)}_{k|k-1})\\ \boldsymbol{c}_{k|k-1}=\eta\alpha(\boldsymbol{d}^{(1)}_{k|k-1}-2\boldsymbol{d}^{(2)}_{k|k-1}+\boldsymbol{d}^{(3)}_{k|k-1})\end{cases} \tag{21}$$

where $\eta=\alpha/2(1-\alpha)^2$; $\kappa_1=6-5\alpha$; $\kappa_2=2(5-4\alpha)$; and $\kappa_3=4-3\alpha$.

The above process is represented by $\boldsymbol{g}$:

$$\boldsymbol{d}_{k|k-1}=\boldsymbol{g}(\hat{\boldsymbol{d}}_{k-T},\hat{\boldsymbol{d}}_{k-T+1},\ldots,\hat{\boldsymbol{d}}_{k-1}) \tag{22}$$

The relation between the forecast $\boldsymbol{d}_{k|k-1}$ and the true value $\boldsymbol{d}_k$ is given by:

$$\boldsymbol{d}_k=\boldsymbol{d}_{k|k-1}+\boldsymbol{\mu}_k \tag{23}$$

where $\boldsymbol{\mu}_k$ is the prediction error of the triple ESM, and its covariance matrix is expressed as $\boldsymbol{\Gamma}_k=E[\boldsymbol{\mu}_k,\boldsymbol{\mu}_k^{\mathrm{T}}]$.

B. CKF with Augmented State Vector

Considering the spatial correlations between the unknown input $\boldsymbol{d}_k$ and the state $\boldsymbol{x}_k$, an augmented state vector is defined as:

$$\boldsymbol{x}_{a,k}=[\boldsymbol{x}_k^{\mathrm{T}},\boldsymbol{d}_k^{\mathrm{T}}]^{\mathrm{T}} \tag{24}$$

Then, $\boldsymbol{d}_k$ is estimated together with $\boldsymbol{x}_k$ by the augmented-state CKF.

Specifically, with the estimated states at time step $k-1$ that have a mean $\hat{\boldsymbol{x}}_{a,k-1}=[\hat{\boldsymbol{x}}_{k-1}^{\mathrm{T}},\hat{\boldsymbol{d}}_{k-1}^{\mathrm{T}}]^{\mathrm{T}}$ and a covariance matrix $\boldsymbol{\Sigma}_{a,k-1}$, $2n$ weighted sigma points are generated as:

$$\boldsymbol{x}^i_{a,k-1}=\begin{bmatrix}\boldsymbol{x}^i_{k-1}\\ \boldsymbol{d}^i_{k-1}\end{bmatrix}=\hat{\boldsymbol{x}}_{a,k-1}\pm\left(\sqrt{n\boldsymbol{\Sigma}_{a,k-1}}\right)_i\quad i=1,2,...,n \tag{25}$$

Subsequently, $\boldsymbol{x}^i_{a,k|k-1}$ is propagated through the nonlinear models $\boldsymbol{f}$ and $\boldsymbol{g}$ to obtain the transformed samples as:

$$\boldsymbol{x}^i_{a,k|k-1}=\begin{bmatrix}\boldsymbol{x}^i_{k|k-1}\\ \boldsymbol{d}^i_{k|k-1}\end{bmatrix}=\begin{bmatrix}\boldsymbol{f}(\boldsymbol{x}^i_{k-1},\boldsymbol{u}_{k-1})+\boldsymbol{G}\hat{\boldsymbol{d}}_{k-1})\\ \boldsymbol{g}(\hat{\boldsymbol{d}}_{k-T},\hat{\boldsymbol{d}}_{k-T+1},...,\hat{\boldsymbol{d}}^i_{k-1})\end{bmatrix} \tag{26}$$

And the predicted state vector $\boldsymbol{x}_{a,k|k-1}$ and its covariance matrix $\boldsymbol{\Sigma}_{a,k|k-1}$ are calculated by:

$$\boldsymbol{x}_{a,k|k-1}=\begin{bmatrix}\boldsymbol{x}_{k|k-1}\\ \boldsymbol{d}_{k|k-1}\end{bmatrix}=\frac{1}{2n}\sum_{i=1}^{2n}\boldsymbol{x}^i_{a,k|k-1} \tag{27}$$

$$\boldsymbol{\Sigma}_{a,k|k-1}=\frac{1}{2n}\sum_{i=1}^{2n}(\boldsymbol{x}^i_{a,k|k-1}-\boldsymbol{x}_{a,k|k-1})(\boldsymbol{x}^i_{a,k|k-1}-\boldsymbol{x}_{a,k|k-1})^{\mathrm{T}}+\begin{bmatrix}\boldsymbol{\Theta}_k & \\ & \boldsymbol{\Gamma}_k\end{bmatrix} \tag{28}$$

where $\boldsymbol{\Sigma}_{a,k|k-1}=[\boldsymbol{\Sigma}_{xx},\boldsymbol{\Sigma}_{xd};\boldsymbol{\Sigma}_{xd}^{\mathrm{T}},\boldsymbol{\Sigma}_{dd}]$, $\boldsymbol{\Sigma}_{xx}$ and $\boldsymbol{\Sigma}_{dd}$ are the covariance matrices of $\boldsymbol{x}_{k|k-1}$ and $\boldsymbol{d}_{k|k-1}$, respectively, both containing information from previous time steps, and $\boldsymbol{\Sigma}_{xd}$ is the cross-covariance matrix of $\boldsymbol{d}$ and $\boldsymbol{x}$ that contains their spatial correlation information.

Then, the propagated sigma points of the predicted measurement $\boldsymbol{z}^i_{k|k-1}$ and their mean $\boldsymbol{z}_{k|k-1}$ are obtained as:

$$\begin{cases}\boldsymbol{z}^i_{k|k-1}=\boldsymbol{h}(\boldsymbol{x}^i_{k|k-1},\boldsymbol{u}_k)\\ \boldsymbol{z}_{k|k-1}=\dfrac{1}{2n}\displaystyle\sum_{i=1}^{2n}\boldsymbol{z}^i_{k|k-1}\end{cases} \tag{29}$$

And the covariance matrix $\boldsymbol{\Sigma}^{zz}_{k|k-1}$ of the predicted measurement error and cross-covariance $\boldsymbol{\Sigma}^{x_a z}_{k|k-1}$ are given by:

$$\boldsymbol{\Sigma}^{zz}_{k|k-1}=\frac{1}{2n}\sum_{i=1}^{2n}(\boldsymbol{z}^i_{k|k-1}-\boldsymbol{z}_{k|k-1})(\boldsymbol{z}^i_{k|k-1}-\boldsymbol{z}_{k|k-1})^{\mathrm{T}}+\boldsymbol{\Lambda}_k \tag{30}$$

$$\boldsymbol{\Sigma}^{x_a z}_{k|k-1}=\frac{1}{2n}\sum_{i=1}^{2n}(\boldsymbol{x}^i_{a,k|k-1}-\boldsymbol{x}_{a,k|k-1})(\boldsymbol{z}^i_{k|k-1}-\boldsymbol{z}_{k|k-1})^{\mathrm{T}} \tag{31}$$

where $\boldsymbol{\Sigma}^{x_a z}_{k|k-1}=[\boldsymbol{\Sigma}^{\mathrm{T}}_{xz},\boldsymbol{\Sigma}^{\mathrm{T}}_{dz}]^{\mathrm{T}}$, and $\boldsymbol{\Sigma}_{xz}$ and $\boldsymbol{\Sigma}_{dz}$ are the cross-covariance matrices of the measurement $\boldsymbol{z}_{k|k-1}$ with $\boldsymbol{x}_{k|k-1}$ and $\boldsymbol{d}_{k|k-1}$, respectively, where the spatial correlations between $\boldsymbol{x}_e$ and $\boldsymbol{z}$ are included.

After obtaining the measurement vector $\boldsymbol{z}_k$, the estimated $\hat{\boldsymbol{x}}_{a,k}$ and its covariance matrix $\boldsymbol{\Sigma}_{e,k}$ can be calculated by:

$$\begin{cases}\hat{\boldsymbol{x}}_{a,k}=\boldsymbol{x}_{a,k|k-1}+\boldsymbol{K}_k(\boldsymbol{z}_k-\boldsymbol{z}_{k|k-1})\\ \boldsymbol{\Sigma}_{e,k}=\boldsymbol{\Sigma}_{a,k|k-1}-\boldsymbol{K}_k\boldsymbol{\Sigma}^{zz}_{k|k-1}\boldsymbol{K}_k^{\mathrm{T}}\end{cases} \tag{32}$$

where $\boldsymbol{K}_k=\boldsymbol{\Sigma}^{x_a z}_{k|k-1}(\boldsymbol{\Sigma}^{zz}_{k|k-1})^{-1}=[\boldsymbol{\Sigma}^{\mathrm{T}}_{xz},\boldsymbol{\Sigma}^{\mathrm{T}}_{dz}]^{\mathrm{T}}(\boldsymbol{\Sigma}^{zz}_{k|k-1})^{-1}$ is the filtering gain, which determines the degree to which the measurement vector $\boldsymbol{z}_k$ modifies $\boldsymbol{x}_{k|k-1}$ and $\boldsymbol{d}_{k|k-1}$. Then, the process returns to (25) to estimate the states of the next time step.

Remark: the prediction $\boldsymbol{d}_{k|k-1}$ by the ESM may be inaccurate when there is a sudden change in $\boldsymbol{d}_k$, which is inevitable because disturbances cannot be reflected in the historical data. However, it can be observed from (25)-(32) that the pre-

diction step and the filtering step of CKF are executed alternately; hence, the cross-correlations of the dynamic state $\boldsymbol{x}$, unknown inputs $\boldsymbol{d}$, and measurement vector $\boldsymbol{z}$ can be used to correct $\boldsymbol{d}_{k|k-1}$ and yield a more accurate estimation of unknown inputs.

C. Adaptive Measurement Interpolation

Owing to discrete measurements and numerical computation, the system dynamic equations in (9) should be discretized into (12). The integral of both sides of the differential equations in (9) during $[t_{k-1}, t_k]$ is calculated as:

$$\int_{t_{k-1}}^{t_k} \dot{\boldsymbol{x}}(t)\mathrm{d}t = \boldsymbol{x}_k - \boldsymbol{x}_{k-1} = \int_{t_{k-1}}^{t_k} \boldsymbol{f}(\boldsymbol{x}(t), \boldsymbol{u}(t))\mathrm{d}t \tag{33}$$

$$\boldsymbol{x}_k = \boldsymbol{x}_{k-1} + \int_{t_{k-1}}^{t_k} \boldsymbol{f}(\boldsymbol{x}(t), \boldsymbol{u}(t))\mathrm{d}t \tag{34}$$

Both the numerical integration approach and the step size Δh can affect the integral accuracy in (34), but the latter has a larger impact for the DFIG, which has fast dynamics owing to its small capacity and power electronic converters. The value of Δh of the DSE is usually consistent with the PMU reporting rate, i.e., $\Delta h = 0.02$ s. However, this step size may not satisfy the requirements of the DSE for the DFIG. Figure 3 presents the comparison of the rotor speed ω_r of a synchronous generator (SG) and a DFIG in the same system with a short-circuit fault. ω_r of the DFIG fluctuates considerably within a step size Δh, which is not the case for the SG. Therefore, the dynamic states of the DFIG are difficult to predict within a step size $\Delta h = 0.02$ s and may lead to the divergence of the DSE.

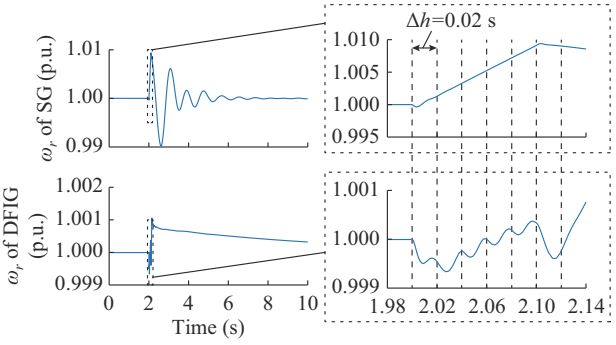

Fig. 3. Comparison between ω_r of SG and DFIG.

Reducing the step size Δh is an effective way to improve the accuracy of numerical integration. However, it is difficult to improve significantly the reporting rate of PMUs because of the restrictions of computing power and communication technology. An alternative approach is the linear interpolation of the measurements.

The interpolation parameter L is defined as the number of pseudo-measurements added between two consecutive measurement samples. The value of L in [16] is simply set to be 10 throughout the DSE process. However, when there is no fault, the DFIG states are stable, and accurate state prediction can be made with a small L; when a fault occurs, the DFIG dynamic states will fluctuate owing to the unbalanced power flow caused by the fault, and L needs to be increased to reduce the discretization error of the CKF prediction step. Therefore, L is expected to change adaptively. Hence, an adaptive approach based on the LTE is proposed to achieve a good tradeoff between the computing time and the estimation accuracy.

First, the LTE is defined. Let $\boldsymbol{x}(t)$ denote the function of the state vector $\boldsymbol{x}$ in (9) with respect to time t, and the p-order Taylor expansion of $\boldsymbol{x}(t)$ is performed at t_{k-1} with $\boldsymbol{x}(t_{k-1})$ represented by $\boldsymbol{x}_{k-1}$:

$$\boldsymbol{x}(t) = \boldsymbol{x}_{k-1} + \dot{\boldsymbol{x}}_{k-1}(t - t_{k-1}) + \ldots + \frac{\boldsymbol{x}_{k-1}^{(p)}}{p!}(t - t_{k-1})^p + o((t - t_{k-1})^p) \tag{35}$$

Let $t = t_k$ and $\Delta h = t_k - t_{k-1}$, and the differential equations in (9) are substituted for $\dot{\boldsymbol{x}}_{k-1}$. Then, $\boldsymbol{x}_k$ is expressed as:

$$\boldsymbol{x}_k = \boldsymbol{x}_{k-1} + \boldsymbol{f}(\boldsymbol{x}_{k-1}, \boldsymbol{u}_{k-1})\Delta h + \ldots + \frac{\boldsymbol{f}^{(p-1)}(\boldsymbol{x}_{k-1}, \boldsymbol{u}_{k-1})}{p!}\Delta h^p + o(\Delta h^p) \tag{36}$$

Take the Euler approach [29] as an example. Let $p = 1$, and we can obtain:

$$\boldsymbol{x}_k = \boldsymbol{x}_{k-1} + \boldsymbol{f}(\boldsymbol{x}_{k-1}, \boldsymbol{u}_{k-1})\Delta h + o(\Delta h) \tag{37}$$

$$\boldsymbol{x}_k^{Euler} = \boldsymbol{x}_{k-1} + \boldsymbol{f}(\boldsymbol{x}_{k-1}, \boldsymbol{u}_{k-1})\Delta h \tag{38}$$

where $\boldsymbol{x}_k^{Euler}$ is the state prediction vector calculated using the Euler approach. $o(\Delta h)$ in (39) is defined as the LTE of the Euler approach, which has first-order accuracy because $p = 1$.

$$o(\Delta h) = \boldsymbol{x}_k - \boldsymbol{x}_k^{Euler} \tag{39}$$

The LTE can reflect the discretization error, and hence can be used as an index to adjust the interpolation parameter L. However, the true state vector $\boldsymbol{x}_k$ is not available in practice, and thus the LTE must be estimated.

Consider two discretization approaches A and B that have p- and q-order accuracy, respectively.

$$o(\Delta h^p) = \boldsymbol{x}_k - \boldsymbol{x}_k^A \tag{40}$$

$$o(\Delta h^q) = \boldsymbol{x}_k - \boldsymbol{x}_k^B \tag{41}$$

where $\boldsymbol{x}_k^A$ and $\boldsymbol{x}_k^B$ are the state prediction vectors calculated using approaches A and B, respectively; q is much larger than p. Then, subtracting (40) from (41) yields:

$$\boldsymbol{x}_k^A - \boldsymbol{x}_k^B = o(\Delta h^p) - o(\Delta h^q) \tag{42}$$

where $o(\Delta h^q)$ is much smaller than $o(\Delta h^p)$. Then, we can obtain:

$$o(\Delta h^p) \approx o(\Delta h^p) - o(\Delta h^q) = \boldsymbol{x}_k^A - \boldsymbol{x}_k^B \tag{43}$$

Formula (43) indicates that the LTE of the discrete approach A with p-order accuracy can be estimated by $\boldsymbol{x}_k^A - \boldsymbol{x}_k^B$.

Then, L is determined based on the estimation of the LTE. If the step size changes from Δh to $\Delta h/L$, the LTE of the discretization approach A with p-order accuracy becomes:

$$o((\Delta h/L)^p) = o(\Delta h^p)/L^p \tag{44}$$

The following definition is given:

$$\boldsymbol{err}_{local,k} = o(\Delta h^p) = \boldsymbol{x}_k^A - \boldsymbol{x}_k^B \tag{45}$$

And the maximum tolerance is represented by ε. Then, (46) should be satisfied to determine L.

$$\begin{cases} o(h^p)/L^p \approx \max|\boldsymbol{err}_{local,k}|/L^p \le \varepsilon \\ L \ge \sqrt[p]{\max|\boldsymbol{err}_{local,k}|/\varepsilon} \end{cases} \tag{46}$$

The result is then rounded up to an integer to obtain L adaptively as:

$$L = \left\lceil \sqrt[p]{\max|\boldsymbol{err}_{local\_k}|/\varepsilon} \right\rceil \tag{47}$$

Remark: the larger the q of approach B, the more accurate is the estimation of the LTE of approach A. However, a discretization approach with high-order accuracy is usually computationally inefficient, which is not suitable for the DSE that operates in real time. Moreover, the objective of AICKF-UI is not to estimate the LTE accurately, but to realize the adaptive adjustment of L when the discretization error based on Δh is unacceptable. Therefore, the third-order Runge-Kutta (3-RK) approach with $q=3$ [30] in (48) is used in this paper to estimate the LTE of 2-RK with $p=2$, and then L is determined by (47).

$$\begin{cases} \boldsymbol{x}_k = \boldsymbol{x}_{k-1} + (\Delta\boldsymbol{x}_1 + 4\Delta\boldsymbol{x}_2 + \Delta\boldsymbol{x}_3)/6 \\ \Delta\boldsymbol{x}_1 = \boldsymbol{f}(\hat{\boldsymbol{x}}_{k-1}, \boldsymbol{u}_{k-1})\Delta h \\ \Delta\boldsymbol{x}_2 = \boldsymbol{f}(\hat{\boldsymbol{x}}_{k-1} + \Delta\boldsymbol{x}_1/2, (\boldsymbol{u}_{k-1} + \boldsymbol{u}_k)/2)\Delta h \\ \Delta\boldsymbol{x}_3 = \boldsymbol{f}(\hat{\boldsymbol{x}}_{k-1} + (-\Delta\boldsymbol{x}_1 + 2\Delta\boldsymbol{x}_2)/2, \boldsymbol{u}_k)\Delta h \end{cases} \tag{48}$$

D. Procedure of AICKF-UI

The flowchart in Fig. 4 illustrates the execution process of the AICKF-UI visually. The proposed approach comprises four steps. In *Step 0*, the AICKF-UI is initialized, and the mean value $\boldsymbol{x}_0$ and covariance matrix $\boldsymbol{\Sigma}_0$ of the states are set up at $k=0$. In *Step 1*, the real PMU measurement interval is input at time step k, and the parameter L is calculated by the proposed adaptive measurement interpolation approach (40)-(47). Then, j is set to be 1. In *Step 2*, the states and unknown inputs are predicted by (25)-(28). The measurement filtering step given by (29)-(32) is performed in *Step 3*. Then, a logical judgment is required: if $j<L$, let $j=j+1$, and return to *Step 2*; if $j=L$, let $k=k+1$, and return to *Step 1*.

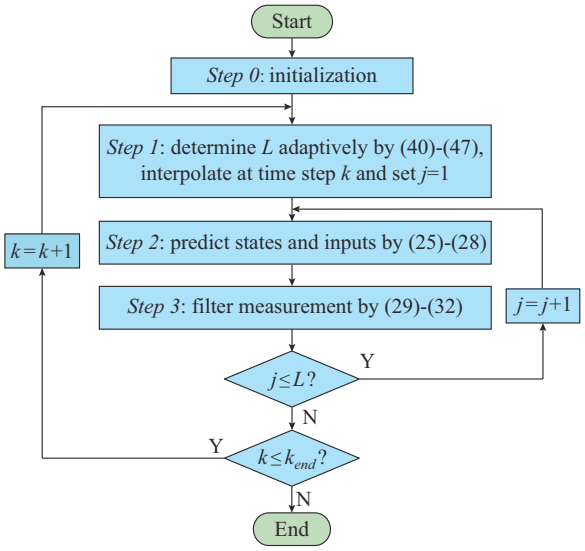

Fig. 4. Flowchart of AICKF-UI.

IV. Case Studies

To evaluate the performance of the proposed AICKF-UI approach, a DFIG-based wind farm and modified IEEE 39-bus system with a group of lumped DFIGs are utilized to generate the simulated PMU data that mimic the real system responses to different disturbances. The simulation is performed using MATLAB/Simulink R2020a on a desktop computer with the following specifications: Intel(R) Core(TM) i7-10700K (8 cores) CPU @ 3.80 GHz, 16 GB RAM (DDR4), and 64-bit Windows 10 operating system.

A. Simulation and DSE Settings

The maximum simulation time step in MATLAB/Simulink is set to be 0.001 s, and all simulation cases last for 10 s. To mimic the field measurements from PMUs, the simulation data are sampled 50 times per second, i.e., $\Delta h=0.02$ s, and zero mean Gaussian noise that accounts for 1% of the original signal amplitude is added. Then, the measurements are used in the DSE to estimate the dynamic states and unknown inputs of the DFIG. In the DSE, the covariance matrix $\boldsymbol{\Lambda}$ of the measurement noise is set to be $10^{-4}\boldsymbol{I}_{m\times m}$ according to the added measurement noise. As the system has unknown inputs, the diagonal component values of the system process noise covariance matrix $\boldsymbol{\Theta}$ associated with the unknown inputs are set to be 10^{-4}, which are 100 times larger than those associated with the state transition model in (12). The maximum tolerance ε of the AICKF-UI approach is set to be 10^{-3}. In addition, the maximum error (ME) and root-mean-square error (RMSE) are defined in (49) and (50), respectively, to quantify the prediction or estimation errors.

$$ME(\boldsymbol{x}_{i,k}) = \max\{|\boldsymbol{x}_{i,k} - \boldsymbol{x}_{i,k}^{true}|, i=1,2,\ldots,n\} \tag{49}$$

$$RMSE(\boldsymbol{x}_i) = \sqrt{\frac{1}{T_s}\sum_{k=1}^{T_s}(\boldsymbol{x}_{i,k} - \boldsymbol{x}_{i,k}^{true})^2} \tag{50}$$

where $\boldsymbol{x}_{i,k}$ is the i^{th} element of the predicted state vector $\boldsymbol{x}_{k|k-1}$ or the estimated state vector $\hat{\boldsymbol{x}}_k$ at time step k; $\boldsymbol{x}_{i,k}^{true}$ is the corresponding true value; and T_s is the length of the measurement data.

Moreover, to determine a proper smoothing factor α of the ESM, mRMSE, which quantifies the overall estimation error, is defined in (51) based on the RMSE. N is the dimension of the extended state vector $\boldsymbol{x}_e$. Considering that α lies between 0 and 1, $\alpha=0, 0.1, \ldots, 1$ (i.e., the interval is 0.1) are employed for the simulation data of both test systems. It is observed that the mRMSE values decrease as α increases, and they do not change significantly when $\alpha\ge0.6$. Therefore, $\alpha=0.7$ is used in this paper.

$$mRMSE = \frac{1}{N}\sum_{i=1}^{N} RMSE(\boldsymbol{x}_i) \tag{51}$$

B. Results for DFIG-based Wind Farm

A DFIG-based wind farm composed of 16 DFIG units is built in MATLAB/Simulink, as shown in Fig. 5. The parameters of a 1.5 MW DFIG unit are listed in Table I. The measurements of each DFIG unit are synchronously uploaded to the master station of the measurement system, and then, the

DSE for each DFIG can be performed using AICKF-UI. Owing to space limitation, only the estimated results of DFIG w_{31} are utilized for illustration. The mean estimated RMSE values of each state of all the DFIGs in the wind farm are given in the form of tables.

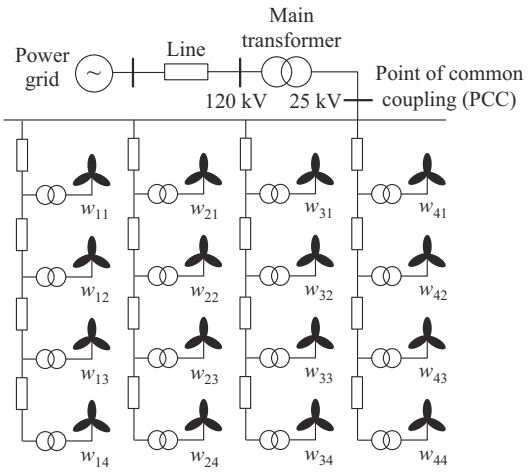

Fig. 5. Topological structure of wind farm.

TABLE I
PARAMETERS OF A 1.5 MW DFIG UNIT

Parameter	Value	Parameter	Value
$P_{m,nom}$	1.5 MW	$P_{e,nom}$	1.67 MW
K_N	0.73 p.u.	$C_{p,nom}$	0.48 p.u.
ω_{nom}	1.2 p.u.	λ_{nom}	8.1 p.u.
$V_{\omega,nom}$	12 m/s	H_g	5.04 s
F	0.01	L_m	2.9 p.u.
R_s	0.00706 p.u.	L_{ls}	0.171 p.u.
R_r	0.005 p.u.	L_{lr}	0.156 p.u.
R_g	0.0015 p.u.	L_g	0.15 p.u.
R_c	0.075 p.u.	ω_s	1 p.u.

1) Effectiveness Test of Measurement Interpolation

This subsection compares the performance of the proposed AICKF-UI approach and CKF-UI without measurement interpolation. The wind speed variation of DFIG w_{31} is shown in Fig. 6. A step change at 2 s and a sinusoidal variation at 2-6 s for the wind speed are set to test the performance of the AICKF-UI approach under quasi-steady-state condition.

The step size of CKF-UI is fixed as the PMU measurement interval $\Delta h = 0.02$ s, and 2-RK and 3-RK are used as the discretization approaches to evaluate the influence of different numerical approaches on the DSE. Note that the discretization approach adopted by AICKF-UI is still 2-RK, but its step size is $\Delta h/L$. Figure 7(a) shows the comparison of ME for $\boldsymbol{x}_{k|k-1}$ by different approaches.

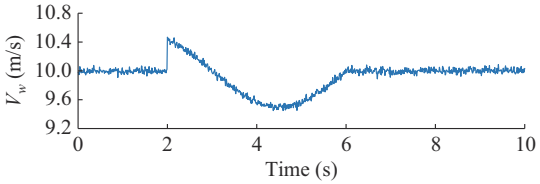

Fig. 6. Wind speed variation of DFIG w_{31}.

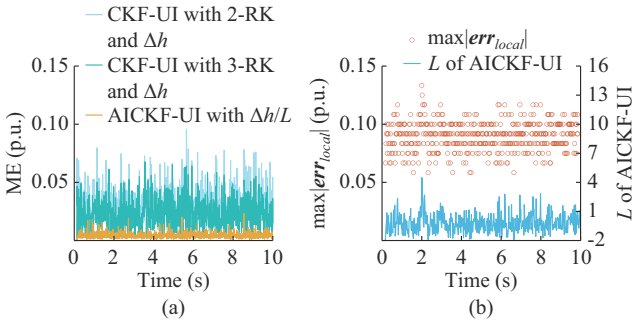

Fig. 7. Evaluation of state prediction accuracy by different approaches. (a) Comparison of ME for $\boldsymbol{x}_{k|k-1}$. (b) max|$\boldsymbol{err}_{local}$| and interpolation parameter L of AICKF-UI.

The ME of CKF-UI with 3-RK is smaller than that of CKF-UI with 2-RK, as the former has higher discretization accuracy. However, the ME of AICKF-UI is much smaller despite the use of 2-RK, because the measurement interpolation considerably reduces the step size, and thus the discretization error decreases. The variations of max|$\boldsymbol{err}_{local}$| in (46) and the interpolation parameter L of AICKF-UI are shown in Fig. 7(b). The value of L mainly changes in the range of 6 to 10, and the step size of AICKF-UI changes according to $\Delta h/L$. The change in the wind speed has no obvious influence on L because it corresponds to a quasi-steady-state disturbance.

The mean RMSE of estimated states and unknown inputs of all the DFIGs are listed in Table II, and the estimated states and unknown inputs of DFIG w_{31} are shown in Fig. 8. In the case of wind speed fluctuation, AICKF-UI can accurately estimate the DFIG states and unknown inputs owing to measurement interpolation, whereas the estimation results of CKF-UI approach have a large deviation. Therefore, for a DFIG with fast dynamics, a smaller Δh is more beneficial to the DSE than discretization approaches of higher-order accuracy.

TABLE II
MEAN RMSE OF ESTIMATED STATES AND UNKNOWN INPUTS OF ALL DFIGS

Approach	Mean RMSE of $\boldsymbol{x}$						Mean RMSE of $\boldsymbol{d}$				
	ω_r	ψ_{dr}	ψ_{qr}	ψ_{ds}	ψ_{qs}	i_{dg}	i_{qg}	u_{dr}	u_{qr}	u_{dg}	u_{qg}
CKF with 2-RK and Δh	0.0036	0.0262	0.0353	0.0679	0.0553	0.0409	0.0356	0.0081	0.0072	0.0097	0.0096
CKF with 3-RK and Δh	0.0024	0.0215	0.0332	0.0318	0.0357	0.0215	0.0167	0.0068	0.0062	0.0075	0.0088
AICKF-UI with $\Delta h/L$	0.0012	0.0067	0.0095	0.0115	0.0193	0.0112	0.0096	0.0022	0.0026	0.0048	0.0051

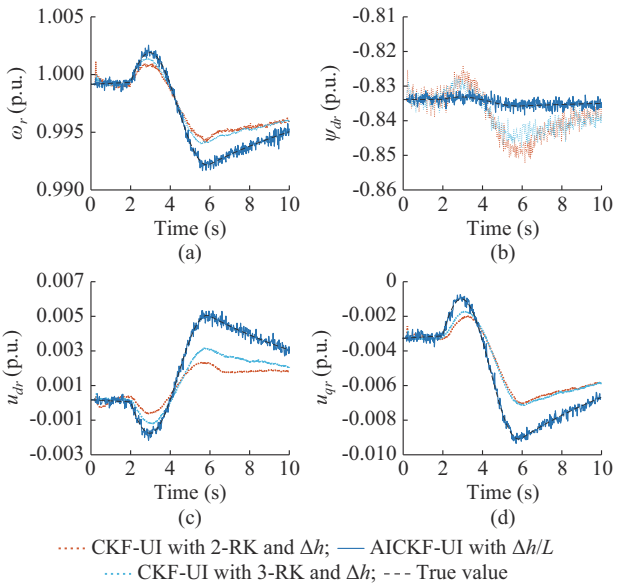

Fig. 8. Estimated states and unknown inputs of DFIG w_{31}. (a) Rotor speed ω_r. (b) Rotor flux ψ_{dr}. (c) Rotor voltage u_{dr}. (d) Rotor voltage u_{qr}.

2) Comparison of Results of Proposed AICKF-UI and ICKF-UI with Different Constant L Values

To demonstrate the advantages of the proposed AICKF-UI approach over the interpolation-based CKF-UI (ICKF-UI) with a constant L, the value of L in ICKF-UI is set to be 1, 3, 7, 12, and 20, and the estimation results of ICKF-UI are compared with those of AICKF-UI. A 10% voltage drop is applied to the PCC bus of the wind farm at 2 s, which will not activate the LVRT control strategies of the DFIG. The fault lasts for 500 ms.

Figure 9(a) shows the mean ME for $\boldsymbol{x}_{k|k-1}$ of different L values. The reduction in the mean ME with the increase in L further proves the effect of the measurement interpolation on reducing the discretization error.

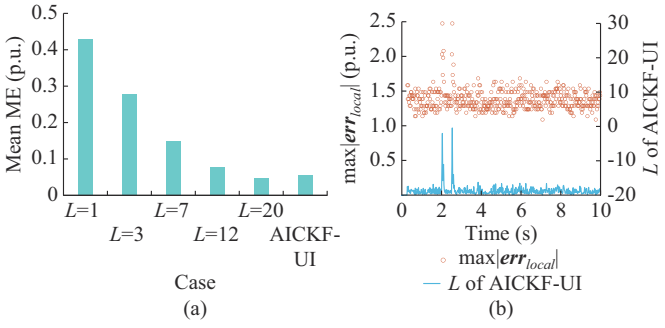

Fig. 9. Evaluation of state prediction accuracy by different approaches. (a) Comparison of mean ME for $\boldsymbol{x}_{k|k-1}$ of different L values. (b) max$|\boldsymbol{err}_{local}|$ and interpolation parameter L of AICKF-UI.

Moreover, the mean ME of AICKF-UI is close to that of ICKF-UI with $L=20$, but the value of L of the former is usually small, as shown in Fig. 9(b), which results in the variations of max$|\boldsymbol{err}_{local}|$ and the interpolation parameter L of AICKF-UI. The value of L mainly changes from 5 to 12, but it increases to more than 20 around 2 s and 2.5 s, which indicates that the discretization error increases during the fault, and that the proposed approach can change L adaptively.

Figure 10 shows the estimation results of the dynamic states ω_r and ψ_{dr} and the unknown inputs u_{dr} and u_{qr} of DFIG w_{31}. The DSE based on ICKF-UI with $L=1$ is terminated because of the nonpositive definite state covariance matrix, and thus its estimation results are not shown here. The mean RMSE values of the estimation results of all the DFIGs and mean computing time of single step are listed in Table III. The estimation errors of ICKF-UI with both $L=3$ and 7 are large, particularly during the fault. The estimated results of ICKF-UI with $L=20$ track the true states well, and the unknown inputs are also estimated accurately; however, owing to the large interpolation parameter L, the mean computing time of a single step exceeds the PMU measurement interval (20 ms), and thus is impractical.

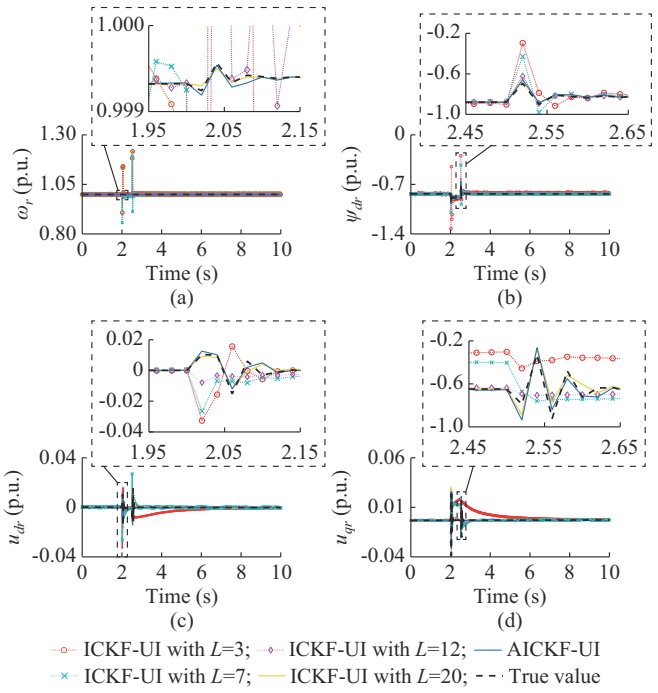

Fig. 10. Estimation results of dynamic states ω_r and ψ_{dr} and unknown inputs u_{dr} and u_{qr} of DFIG w_{31}. (a) Rotor speed ω_r. (b) Rotor flux ψ_{dr}. (c) Rotor voltage u_{dr}. (d) Rotor voltage u_{qr}.

By contrast, the mean RMSE of AICKF-UI is close to that of ICKF with $L=20$ but with a shorter computing time. This demonstrates that the proposed approach is more efficient by changing L adaptively in different situations.

Furthermore, note that the value of L of AICKF-UI in Fig. 9(b) is larger than 20 at some time steps, and consequently, the single-step computing time (SSCT) of these time steps may exceed the PMU measurement interval. Therefore, it is necessary to add an upper limit for the value L of AICKF-UI. A reasonable upper limit will have no impact on the estimation accuracy because the accuracy improvement is tiny when L increases to a certain level, as shown in Fig. 9(a). The actual SSCT for the cases of $L=16$, 17, 18, 19, and 20 is measured, and the corresponding mean values and standard deviation (STD) of SSCT are listed in Table IV. When $L=17$, the mean SSCT is 19.581 ms, which is shorter than the PMU measurement interval. Thus, 17 is chosen as the

upper limit for the interpolation parameter L in AICKF-UI in the following cases. The mean RMSE of all DFIGs for AICKF-UI with an upper limit is shown in Table V, and the estimation accuracy does not decrease significantly compared with the results of AICKF-UI without a limit.

TABLE III
MEAN RMSE VALUES OF ESTIMATION RESULTS OF ALL DFIGS AND MEAN COMPUTING TIME OF SINGLE STEP

Approach	Mean RMSE of $\boldsymbol{x}$							Mean RMSE of $\boldsymbol{d}$				Time (ms)
	ω_r	ψ_{dr}	ψ_{qr}	ψ_{ds}	ψ_{qs}	i_{dg}	i_{qg}	u_{dr}	u_{qr}	u_{dg}	u_{qg}	
ICKF ($L=3$)	0.0329	0.0487	0.1082	0.2052	0.3146	0.2539	0.1872	0.0178	0.0225	0.0212	0.0365	3.511
ICKF ($L=7$)	0.0187	0.0191	0.0554	0.0628	0.1293	0.1432	0.1027	0.0108	0.0153	0.0129	0.0145	8.897
ICKF ($L=12$)	0.0032	0.0045	0.0193	0.0133	0.0265	0.0587	0.0413	0.0069	0.0065	0.0078	0.0095	14.153
ICKF ($L=20$)	0.0008	0.0018	0.0058	0.0067	0.0087	0.0015	0.0017	0.0046	0.0031	0.0039	0.0041	25.518
AICKF-UI	0.0009	0.0029	0.0066	0.0067	0.0074	0.0018	0.0016	0.0043	0.0025	0.0042	0.0033	11.466

TABLE IV
MEAN VALUES AND STD OF SSCT

L	Mean value (ms)	STD
16	17.943	0.489
17	19.581	0.359
18	21.509	0.548
19	23.923	0.492
20	25.518	0.390

TABLE V
MEAN RMSE OF ALL DFIGS FOR AICKF-UI WITH AN UPPER LIMIT

Mean RMSE of $\boldsymbol{x}$ (10^{-3})							Mean RMSE of $\boldsymbol{d}$ (10^{-3})			
ω_r	ψ_{dr}	ψ_{qr}	ψ_{ds}	ψ_{qs}	i_{dg}	i_{qg}	u_{dr}	u_{qr}	u_{dg}	u_{qg}
1.1	3.1	7.5	6.8	2.3	2.7	2.0	5.8	2.9	4.3	3.8

3) Performance of Unknown Input Estimation Under Severe Voltage Drop

In the event of a severe voltage drop, the DFIG control will switch to LVRT control strategies to keep the DFIG connected to the grid, which presents a challenge to the estimation of unknown inputs.

The performance of the proposed AICKF-UI approach in such a situation is evaluated in this subsection. A 70% voltage drop is applied to the PCC bus of the wind farm at 2 s, and the fault is cleared at 2.5 s.

The LVRT control strategies of DFIG used in the simulation are as follows: the crowbar is switched on at 2.0-2.1 s to protect the DFIG rotor from an overcurrent, and meanwhile the RSC is blocked. As the DFIG becomes an asynchronous generator after the crowbar is switched on, it will absorb more reactive power [23]. The DFIG is also required to provide reactive power support during the fault of a voltage drop. Therefore, the reactive power priority control strategy is enabled at 2.1-2.5 s, and the reactive current reference value $i_{dr,ref}$ is no longer given by the conventional power outer loop [8], but is determined by:

$$i_{dr,ref}=\min[I_{r,\max},1.5(0.9U_{s,nom}-U_{s,fault})] \tag{52}$$

where $I_{r,\max}$ is the maximum allowable current of the RSC; $U_{s,nom}$ is the rated DFIG terminal voltage; and $U_{s,fault}$ is the actual DFIG terminal voltage during the fault.

Figure 11(a) shows the variation of u_{dr} under conventional control and LVRT control, whereas Fig. 11(b) shows that of Q_e under the two control strategies. Figure 11(a) shows that $u_{dr}=0$ when the crowbar is switched on from 2.0 to 2.1 s, but u_{dr} of the conventional control fluctuates considerably. In Fig. 11(b), the DFIG with reactive power priority control outputs more reactive power from 2.1 to 2.5 s, whereas Q_e of the DFIG with conventional control is almost zero. Thus, the DFIG behaves differently when the LVRT control is activated, and it is impractical to consider only conventional control in the DSE. By contrast, the proposed AICKF-UI approach has broad applicability because it regards the outputs of the converter as unknown inputs of the DSE regardless of the specific control strategies of DFIG converter.

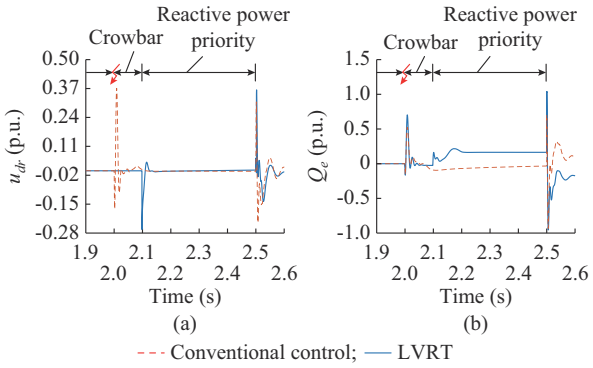

Fig. 11. Comparison of u_{dr} and Q_e under conventional control and LVRT control. (a) Variation of u_{dr}. (b) Variation of Q_e.

The unknown inputs of DFIG w_{31} predicted and estimated by AICKF-UI are compared in Fig. 12. The prediction is accurate when the unknown inputs change smoothly, but there will be a bias for a duration when there is a sudden change caused by a fault, which is inevitable because the ESM is based on historical data. However, the deviation is corrected in the measurement filtering step of AICKF-UI by considering the correlations of the unknown inputs $\boldsymbol{d}_k$, dynamic states $\boldsymbol{x}_k$, and measurements $\boldsymbol{z}_k$. In addition, the measurement interpolation enables multiple corrections of $\boldsymbol{d}_k$ within a measurement interval, which is beneficial to the accurate estimation

of $\boldsymbol{d}_k$. Therefore, the estimated unknown inputs track the true values well even when LVRT control is activated by a severe voltage drop.

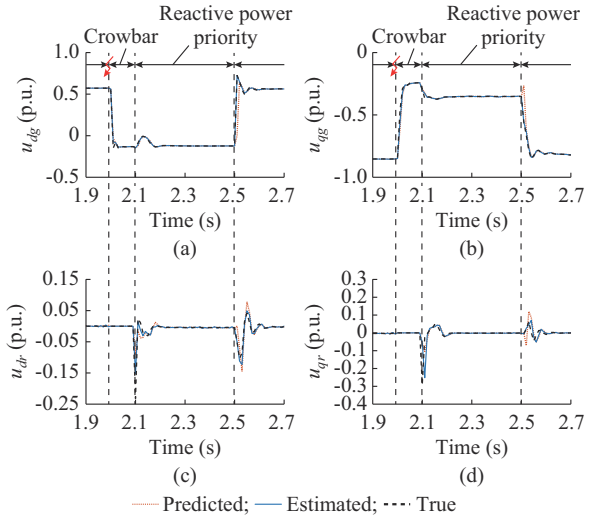

Fig. 12. Unknown inputs of DFIG w_{31} predicted and estimated by AICKF-UI. (a) Grid-side u_{dg} of GSC. (b) Grid-side u_{qg} of GSC. (c) Rotor voltage u_{dr}. (d) Rotor voltage u_{qr}.

Figure 13 shows the estimation results of all the dynamic states of DFIG w_{31}. In the case of a severe voltage drop, the interpolation parameter L increases above 15, which enables AICKF-UI to estimate the states of DFIG w_{31} accurately.

The results of other DFIG units in the wind farm have similar trends, and hence are not shown here to be concise.

C. Results for Modified IEEE 39-bus System

In the case of large-scale systems, the equivalent model of a wind farm is often used to reduce the model order and improve the simulation efficiency. Thus, the DSE can only be developed at the point where the wind farm is connected to the power grid, and only the measurements of the PMU installed at the connection point are available. However, if the DFIG controller model is included in the DSE, it may cause observability problems owing to the existence of too many dynamic states [6]. Moreover, it is a considerable challenge to accurately acquire the equivalent controller parameters. For the equivalent model of the wind farm, the converter outputs do not exist, and thus cannot be measured. By contrast, the proposed AICKF-UI approach considers the converter controller outputs as the unknown inputs of the DSE and eliminates the dependence on the control models and parameters. Therefore, the approach is well suited for this scenario.

The IEEE 39-bus system [9], modified by connecting a group of lumped DFIGs (60 × 1.5 MW) to bus 29, is used to verify the generalization of the proposed approach. Note that the equivalent model of the wind farm in a simulation software still adopts the complete DFIG model. A break line fault is applied from 2 to 3 s by opening the transmission line between buses 28 and 29. Some of the results of the estimated states and unknown inputs of DFIG are shown in Figs. 14 and 15.

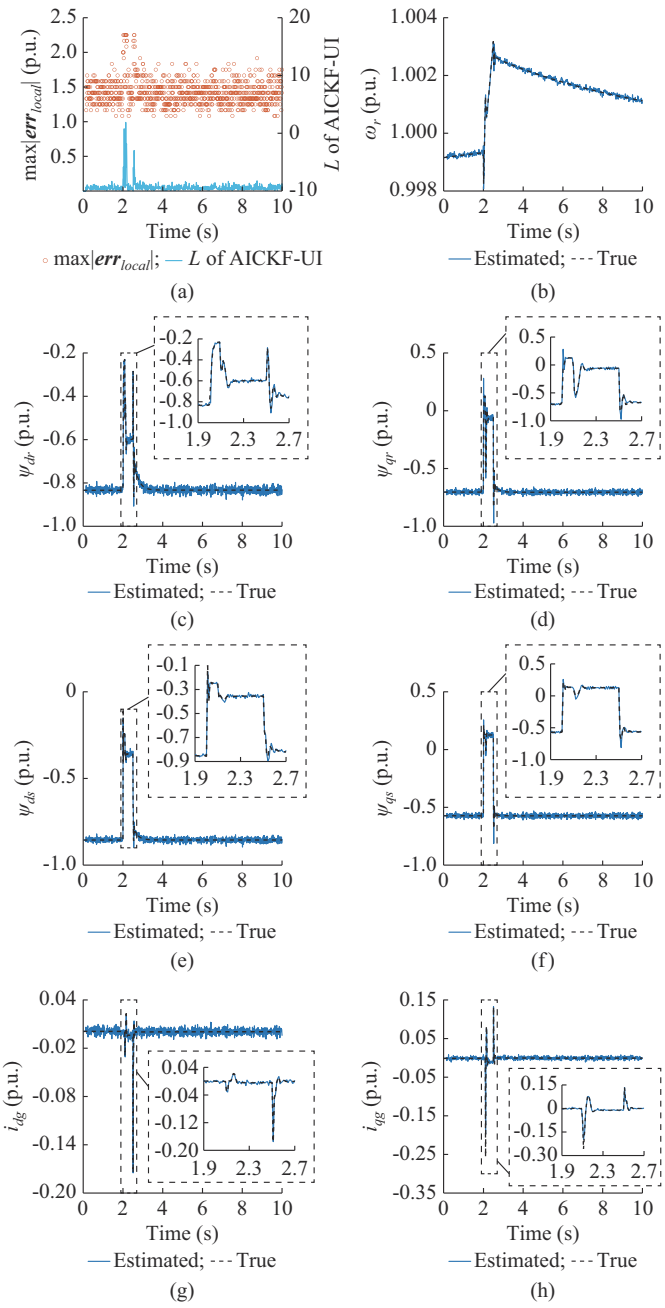

Fig. 13. Estimation results of all dynamic states of DFIG w_{31}. (a) max|$\boldsymbol{err}_{local}$| and interpolation parameter L of AICKF-UI. (b) Rotor speed ω_r. (c) Rotor flux ψ_{dr}. (d) Rotor flux ψ_{qr}. (e) Stator flux ψ_{ds}. (f) Stator flux ψ_{qs}. (g) Grid-side current i_{dg} of GSC. (h) Grid-side current i_{qg} of GSC.

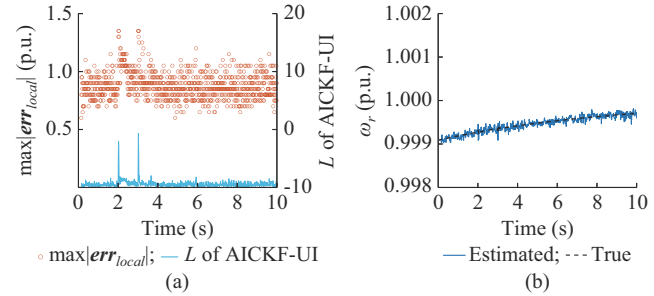

Fig. 14. Estimated states of DFIG. (a) max|$\boldsymbol{err}_{local}$| and interpolation parameter L of AICKF-UI. (b) Rotor speed ω_r.

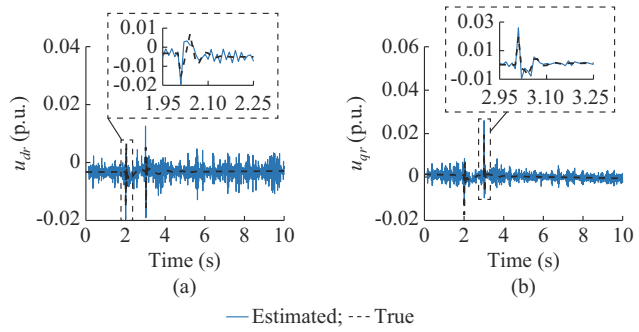

Fig. 15. Estimated unknown inputs of DFIG. (a) Rotor voltage u_{dr}. (b) Rotor voltage u_{qr}.

The value of L of AICKF-UI varies from 5 to 11 in normal situations and increases adaptively to more than 15 when the disconnection fault occurs. As the adaptive measurement interpolation is used, the estimated states in Fig. 14 and the unknown inputs in Fig. 15 of the DFIG track the corresponding true values well, which validate the proposed approach for the equivalent DFIG in a large-scale system.

V. Conclusion

In this paper, an AICKF-UI approach has been developed for estimating the dynamic states of a DFIG. Instead of using the full dynamic model with high complexity, we have proposed to consider the converter controller outputs as the unknown inputs of the DSE and estimated them together with the original DFIG dynamic states using triple ESM and the augmented-state CKF. This eliminates the dependence on different control models.

The discretization process of the continuous system has been analyzed, and an adaptive interpolation approach based on the LTE has been proposed to achieve the desired tradeoff between the computing time and the estimation accuracy. Simulation results show that the proposed AICKF-UI approach can adaptively adjust the interpolation factor based on the variation of the LTE, yielding an accurate estimation of dynamic states and unknown inputs.

Appendix A

The Jacobian matrix of $\boldsymbol{h}_k$ is used to check whether the requirement of $rank(\boldsymbol{H}_k\boldsymbol{G})=rank(\boldsymbol{G})=m$ is met. Therefore, the DFIG measurement function can be expressed as:

$$\boldsymbol{H}_k=\frac{\partial \boldsymbol{h}_k}{\partial \boldsymbol{x}_k}=$$
$$\begin{bmatrix} 0 & -\frac{u_1}{L_{ls}}+\frac{u_1}{\sigma L_{ls}^2} & -\frac{u_2}{L_{ls}}+\frac{u_2}{\sigma L_{ls}^2} & \frac{u_1}{\sigma L_{ls}L_{lr}} & \frac{u_2}{\sigma L_{ls}L_{lr}} & -u_1 & -u_2 \\ 0 & -\frac{u_2}{L_{ls}}+\frac{u_2}{\sigma L_{ls}^2} & \frac{u_1}{L_{ls}}-\frac{u_1}{\sigma L_{ls}^2} & \frac{u_2}{\sigma L_{ls}L_{lr}} & \frac{u_1}{\sigma L_{ls}L_{lr}} & -u_2 & u_1 \\ 0 & \frac{1}{L_{ls}}-\frac{1}{\sigma L_{ls}^2} & 0 & -\frac{1}{\sigma L_{ls}L_{lr}} & 0 & 0 & 0 \\ 0 & 0 & \frac{1}{L_{ls}}-\frac{1}{\sigma L_{ls}^2} & 0 & -\frac{1}{\sigma L_{ls}L_{lr}} & 0 & 0 \end{bmatrix} \quad \text{(A1)}$$

Then, $\boldsymbol{H}_k\boldsymbol{G}$ can be calculated as:

$$\boldsymbol{H}_k\boldsymbol{G}=\begin{bmatrix} \frac{\omega_b\Delta h u_1}{\sigma L_{ls}L_{lr}} & \frac{\omega_b\Delta h u_2}{\sigma L_{ls}L_{lr}} & \frac{u_1\omega_b\Delta h}{L_g} & \frac{u_2\omega_b\Delta h}{L_g} \\ \frac{\omega_b\Delta h u_2}{\sigma L_{ls}L_{lr}} & \frac{\omega_b\Delta h u_1}{\sigma L_{ls}L_{lr}} & \frac{u_2\omega_b\Delta h}{L_g} & -\frac{u_1\omega_b\Delta h}{L_g} \\ -\frac{\omega_b\Delta h}{\sigma L_{ls}L_{lr}} & 0 & 0 & 0 \\ 0 & -\frac{\omega_b\Delta h}{\sigma L_{ls}L_{lr}} & 0 & 0 \end{bmatrix} \quad \text{(A2)}$$

As is clear from the (A2), the row and column vectors of $\boldsymbol{H}_k\boldsymbol{G}$ are all linearly independent, which means that the rank of $\boldsymbol{H}_k\boldsymbol{G}$ is equal to that of $\boldsymbol{G}$ (equal to 4 in the DFIG case of this paper). Therefore, the rank requirement is satisfied and the unknown input vector $\boldsymbol{d}$ can be observed from the selected measurement vector $\boldsymbol{z}$ of the DFIG system.

Appendix B

In the case of nonlinear DFIG system, its augmented state transition equations are represented by:

$$\boldsymbol{x}_{a,k}=\begin{bmatrix}\boldsymbol{x}_k\\ \boldsymbol{d}_k\end{bmatrix}=\begin{bmatrix}\boldsymbol{f}(\boldsymbol{x}_{k-1},\boldsymbol{u}_{k-1})+\boldsymbol{G}\boldsymbol{d}_{k-1}\\ \boldsymbol{g}(\boldsymbol{d}_{k-T},\boldsymbol{d}_{k-T+1},...,\boldsymbol{d}_{k-1})\end{bmatrix} \quad \text{(B1)}$$

where $\boldsymbol{g}$ denotes the transition equations of $\boldsymbol{d}$. Then, the first-order approximation for matrices $\boldsymbol{F}_{a,k}$ and $\boldsymbol{H}_{a,k}$ can be calculated at a given time step k. $\boldsymbol{H}_{a,k}=[\boldsymbol{H}_k,\boldsymbol{0}_{m\times p}]$, the expression of $\boldsymbol{H}_k$ is shown in (A1), and $\boldsymbol{F}_{a,k}$ is expressed as:

$$\begin{cases} \boldsymbol{F}_{a,k}=\begin{bmatrix}\boldsymbol{F}_{fx} & \boldsymbol{F}_{fd}\\ \boldsymbol{F}_{gx} & \boldsymbol{F}_{gd}\end{bmatrix} \\ \boldsymbol{F}_{fx}=\left.\dfrac{\partial \boldsymbol{f}}{\partial \boldsymbol{x}}\right|_{\boldsymbol{x}=\boldsymbol{x}_k} \\ \boldsymbol{F}_{fd}=\left.\dfrac{\partial \boldsymbol{f}}{\partial \boldsymbol{d}}\right|_{\boldsymbol{d}=\boldsymbol{d}_k}=\boldsymbol{G} \\ \boldsymbol{F}_{gx}=\left.\dfrac{\partial \boldsymbol{g}}{\partial \boldsymbol{x}}\right|_{\boldsymbol{x}=\boldsymbol{x}_k}=\boldsymbol{0} \\ \boldsymbol{F}_{gd}=\left.\dfrac{\partial \boldsymbol{g}}{\partial \boldsymbol{d}}\right|_{\boldsymbol{d}=\boldsymbol{d}_k}=\mathrm{diag}(\alpha,\alpha,\alpha,\alpha) \end{cases} \quad \text{(B2)}$$

Then, the observability matrix $\tilde{\boldsymbol{O}}$ can be constructed. The singular value decomposition (SVD) of $\tilde{\boldsymbol{O}}$ is a factorization of the form $\tilde{\boldsymbol{O}}=\boldsymbol{U}\boldsymbol{S}\boldsymbol{V}^{\mathrm{T}}$, where $\boldsymbol{S}$ is given as:

$$\boldsymbol{S}=\mathrm{diag}(\delta_1,\delta_2,...,\delta_n)\quad \delta_1\ge\delta_2\ge...\ge\delta_n \quad \text{(B3)}$$

where δ_i is the singular value of $\tilde{\boldsymbol{O}}$; and the number of the non-zero singular values is equal to $rank(\tilde{\boldsymbol{O}})$. If the smallest singular value (SSV) δ_n of $\tilde{\boldsymbol{O}}$ is non-zero, we can get $rank(\tilde{\boldsymbol{O}})=n$, i.e., the system is observable.

The simulation setups are the same as those used in the second case of the Section IV-B. Analysis results show that the SSV always keeps greater than zero throughout the process and the mean and standard deviation of the SSV of the observability matrices is 1.975 ± 0.046, which means that the SSV of $\tilde{\boldsymbol{O}}$ is always non-zero. Therefore, the DFIG system with the augmented states is considered observable under the selected measurement set.

REFERENCES

[1] H. Zhou, P. Ju, Y. Xue *et al.*, "Probabilistic equivalent model of DFIG-based wind farms and its application in stability analysis," *Journal of Modern Power Systems and Clean Energy*, vol. 4, no. 2, pp. 248-255, Apr. 2016.

[2] R. Xiao, G. Wang, X. Hao *et al.*, "Dynamic state estimation of medium-voltage DC integrated power system with pulse load," *Journal of Modern Power Systems and Clean Energy*, vol. 8, no. 4, pp. 689-698, Jul. 2020.

[3] J. Zhao, M. Netto, Z. Huang *et al.*, "Roles of dynamic state estimation in power system modeling, monitoring and operation," *IEEE Transactions on Power Systems*, vol. 36, no. 3, pp. 2462-2472, May 2020.

[4] M. Rostami and S. Lotfifard, "Distributed dynamic state estimation of power systems," *IEEE Transactions on Industrial Informatics*, vol. 14, no. 8, pp. 3395-3404, Aug. 2018.

[5] Z. Cheng, H. Ren, B. Zhang *et al.*, "Distributed Kalman filter for large-scale power systems with state inequality constraints," *IEEE Transactions on Industrial Electronics*, vol. 68, no. 7, pp. 6238-6247, Jul. 2021.

[6] J. Zhao, A. G. Expósito, Z. Huang *et al.*, "Power system dynamic state estimation: motivations, definitions, methodologies, and future work," *IEEE Transactions on Power Systems*, vol. 34, no. 4, pp. 3188-3198, Jul. 2019.

[7] X. Wang, X. Wei, and Y. Meng, "Experiment on grid-connection process of wind turbines in fractional frequency wind power system," *IEEE Transactions on Energy Conversion*, vol. 30, no. 1, pp. 22-31, Mar. 2015.

[8] S. Yu, K. Emami, T. Fernando *et al.*, "State estimation of doubly fed induction generator wind turbine in complex power systems," *IEEE Transactions on Power Systems*, vol. 31, no. 6, pp. 4935-4944, Nov. 2016.

[9] S. Yu, J. Guo, T. K. Chau *et al.*, "An unscented particle filtering approach to decentralized dynamic state estimation for DFIG wind turbines in multi-area power systems," *IEEE Transactions on Power Systems*, vol. 35, no. 4, pp. 2670-2682, Jul. 2020.

[10] M. Firouzi and G. B. Gharehpetian, "LVRT performance enhancement of DFIG-based wind farms by capacitive bridge-type fault current limiter," *IEEE Transactions on Sustainable Energy*, vol. 9, no. 3, pp. 1118-1125, Jul. 2018.

[11] P. Verma, K. Seethalekshmi, and B. Dwivedi, "A cooperative approach of frequency regulation through virtual inertia control and enhancement of low voltage ride-through in DFIG-based wind farm," *Journal of Modern Power Systems and Clean Energy*, vol. 10, no. 6, pp. 1519-1530, Nov. 2022.

[12] K. Shi, X. Yin, L. Jiang *et al*., "Perturbation estimation based nonlinear adaptive power decoupling control for DFIG wind turbine," *IEEE Transactions on Power Electronics*, vol. 35, no. 1, pp. 319-333, Jan. 2020.

[13] A. M. A. Haidar, K. M. Muttaqi, and M. T. Hagh, "A coordinated control approach for DC link and rotor crowbars to improve fault ride-through of DFIG-based wind turbine," *IEEE Transactions on Industry Applications*, vol. 53, no. 4, pp. 4073-4086, Jul. 2017.

[14] S. Song, P. Wu, Y. Lin *et al*., "A general dynamic state estimation framework for monitoring and control of permanent magnetic synchronous generators-based wind turbines," *IEEE Access*, vol. 9, pp. 72228-72238, May 2021.

[15] S. A. A. Shahriari, M. Raoofat, M. Dehghani *et al*., "Dynamic state estimation of a permanent magnet synchronous generator-based wind turbine," *IET Renewable Power Generation*, vol. 10, no. 9, pp. 1278-1286, Oct. 2016.

[16] G. Anagnostou, L. P. Kunjumuhammed, and B. C. Pal, "Dynamic state estimation for wind turbine models with unknown wind velocity," *IEEE Transactions on Power Systems*, vol. 34, no. 5, pp. 3879-3890, Sept. 2019.

[17] S. Yu, X. Fan, T. K. Chau *et al*., "Square-root sigma-point filtering approach to state estimation for wind turbine generators in interconnected energy systems," *IEEE Systems Journal*, vol. 15, no. 2, pp. 1557-1566, Jun. 2021.

[18] P. Chen, C. Qi, and X. Chen, "Virtual inertia estimation method of DFIG-based wind farm with additional frequency control," *Journal of Modern Power Systems and Clean Energy*, vol. 9, no. 5, pp. 1076-1087, Sept. 2021.

[19] M. Cui, J. Wang, J. Tan *et al*., "A novel event detection method using PMU data with high precision," *IEEE Transactions on Power Systems*, vol. 34, no. 1, pp. 454-466, Jan. 2019.

[20] S. E. Minkoff and N. M. Kridler, "A comparison of adaptive time stepping methods for coupled flow and deformation modeling," *Applied Mathematical Modelling*, vol. 30, no. 9, pp. 993-1009, Sept. 2006.

[21] C. C. Handapangoda, M. Premaratne, L. Yeo *et al*., "Laguerre Runge-Kutta-Fehlberg method for simulating laser pulse propagation in biological tissue," *IEEE Journal on Selected Topics in Quantum Electronics*, vol. 14, no. 1, pp. 105-112, Jan. 2008.

[22] S. Yu, T. Fernando, H. H. Ching Iu *et al*., "Realization of state-estimation-based DFIG wind turbine control design in hybrid power systems using stochastic filtering approaches," *IEEE Transactions on Industrial Informatics*, vol. 12, no. 3, pp. 1084-1092, Jun. 2016.

[23] Z. Din, J. Zhang, Y. Zhu *et al*., "Impact of grid impedance on LVRT performance of DFIG system with rotor crowbar technology," *IEEE Access*, vol. 7, pp. 127999-128008, Aug. 2019.

[24] Y. Wan, "Summary report of wind farm data," Tech. Rep., National Renewable Energy Laboratory, Golden, USA, 2008.

[25] W. Gautschi, *Numerical Analysis*. Boston: Birkhäuser Boston, 2012.

[26] G. Anagnostou and B. C. Pal, "Derivative-free Kalman filtering based approaches to dynamic state estimation for power systems with unknown inputs," *IEEE Transactions on Power Systems*, vol. 33, no. 1, pp. 116-130, Jan. 2018.

[27] M. S. R. Mousavi and B. Boulet, "Estimation of the state variables and unknown input of a two-speed electric vehicle driveline using fading-memory Kalman filter," *IEEE Transactions on Transportation Electrification*, vol. 2, no. 2, pp. 210-220, Jun. 2016.

[28] W. Jiang, X. Wu, and Y. Gong *et al*., "Holt-Winters smoothing enhanced by fruit fly optimization algorithm to forecast monthly electricity consumption," *Energy*, vol. 193, pp. 807-814, Feb. 2020.

[29] D. Simon, *Optimal State Estimation*. Hoboken: Wiley, 2006.

[30] P. Kunder, *Power System Stability and Control*. New York: McGraw-Hill, 1994.

Maolin Zhu received the B.E. degree in electrical engineering and its automation from North China Electric Power University, Beijing, China, in 2018, where he is currently pursuing the Ph.D. degree in electrical engineering. His research interest includes power system dynamic state estimation.

Hao Liu received the Ph.D. degree in electrical engineering from North China Electric Power University, Beijing, China, in 2015. He is currently an Associate Professor with North China Electric Power University. His research interests include synchronized measurement technique, testing and calibration and their applications.

Junbo Zhao received the Ph.D. degree from Virginia Tech, Falls Church, USA, in 2018. He is currently an Assistant Professor with the Department of Electrical and Computer Engineering, University of Connecticut, Storrs, USA. He was an Assistant Professor and a Research Assistant Professor with Mississippi State University, Starkville, USA and Virginia Tech, Blacksburg, USA, from 2019 to 2021 and from 2018 to 2019, respectively. He did the summer internship with Pacific Northwest National Laboratory in 2017. He is the Principal Investigator for a multitude of projects funded by the National Science Foundation, the Department of Energy, National Laboratories, and Eversource Energy. He has published three book chapters and more than 100 peer-reviewed journal and conference papers. His research interests include cyber-physical power system modeling, monitoring, uncertainty quantification, learning, dynamics, stability control, and cyber security with distributed energy resources.

Bendong Tan received the bachelor's and M.S. degrees both in electrical engineering from Wuhan University, Wuhan, China, in 2017 and 2020, respectively. He is now pursuing the Ph.D. degree from the University of Connecticut, Storrs, USA, from 2022. His research interests include power system estimation, monitoring, and stability control.

Tianshu Bi received the Ph.D. degree in electrical and electronic engineering from the University of Hong Kong, Hong Kong, China, in 2002. She is currently a Professor at North China Electric Power University, Beijing, China. Her research interests include power system protection and control, and synchrophasor measurement techniques and their applications.

Samson Shenglong Yu received the master's degree in electrical and electronic engineering and the Ph.D. degree in electrical engineering from The University of Western Australia (UWA), Perth, Australia, in 2014 and 2017, respectively. From 2011 to 2012, he was an Electronics Design and Testing

Engineer. From 2017 to 2019, he was a Postdoctoral Research Fellow with UWA. Since August 2019, he has been an Assistant Professor (Lecturer) with Deakin University, Melbourne, Australia. Since 2015, he has been authored or coauthored more than 80 journal articles, book chapters, and technical reports in highly renowned international publication fora. He has been working with international scholars on a wide range of industrial and research projects in battery technology, electrical faults, technology for future readiness in microgrids, etc. His research interests include systems engineering, system dynamics, power systems, renewable energy integration, applied electronics and control, and nonlinear systems.